Temporal Coarse Graining of CO$_2$ and N$_2$ Diffusion in Zeolite NaKA: From the Quantum Scale to the Macroscopic

Amber Mace,[†] Mikael Leetmaa,[‡] and Aatto Laaksonen*,[†]

[†]Department of Materials and Environmental Chemistry and Berzelii Centre EXSELENT on Porous Materials, Stockholm University, SE-106 91 Stockholm, Sweden

[‡]Department of Physics and Astronomy, Uppsala University, Box 516, SE-751 20 Uppsala, Sweden

S Supporting Information

ABSTRACT: The kinetic CO$_2$-over-N$_2$ sieving capabilities in narrow pore zeolites are dependent on the free-energy barriers of diffusion between the zeolite pores, which can be fine-tuned by altering the framework composition. An *ab initio* level of theory is necessary to accurately compute the energy barriers, whereas it is desirable to predict the macroscopic scale diffusion for industrial applications. Using *ab initio* molecular dynamics on the picosecond time scale, the free-energy barriers of diffusion can be predicted for different local pore properties in order to identify those that are rate-determining for the pore-to-pore diffusion. Specifically, we investigate the effects of the Na$^+$-to-K$^+$ exchange at the different cation sites and the CO$_2$ loading in Zeolite NaKA. These computed energy barriers are then used as input for the Kinetic Monte Carlo method, coarse graining the dynamic simulation steps to the pore-to-pore diffusion. With this approach, we simulate how the identified rate-determining properties as well as the application of skin-layer surface defects affect the diffusion driven uptake in a realistic Zeolite NaKA powder particle model on a macroscopic time scale. Lastly, we suggest a model by combining these effects, which provides an excellent agreement with the experimental CO$_2$ and N$_2$ uptake behaviors presented by Liu et al. (*Chem. Commun.* **2010**, *46*, 4502−4504).
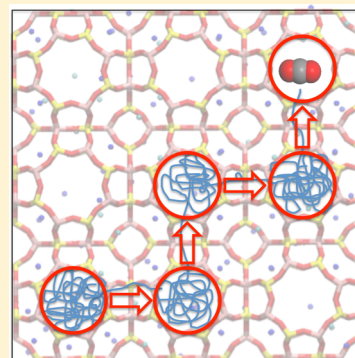
1. INTRODUCTION

Small pore zeolites, such as Zeolite A, have been interesting candidates for carbon capture applications and the separation of CO$_2$ from fluegases due to the material's size-selective sieving capabilities. A particular interest has been in the process of separating CO$_2$ from N$_2$. Here, previous studies have shown that the possibility of tuning the small pore zeolites' sieving properties can provide a diffusionally enhanced CO$_2$-over-N$_2$ selectivity, for example, through ion exchange[1,2] and/or by altering the Si/Al ratio.[3]

Simulating the gas uptake in porous material, where the possibility of reaching an equilibrium uptake at a given time is more or less restricted by the gas molecules' possibility of efficiently reaching all of the material's pores, is not straightforward. This is so because both the thermodynamic aspects, i.e. the affinity between the zeolite pore surface and the gas molecule, as well as dynamic aspects need to taken into account. Many force-field-based modeling studies have been done on these two aspects, separately.[4−12]

Using predetermined force fields is a fast and efficient way to describe the interatomic interactions in molecular simulations. However, the outcome is directly dependent on the quality of the force field. When it comes to gas−zeolite interactions, many force fields have been developed for all-silica zeolites,[13,14] as well as for individual aluminum and extra-framework cation-containing zeolites.[4,7,9,15] However, no force field has been specifically derived for K$^+$-containing zeolites and a reliable and

transferable general zeolite force field is still lacking. In particular, this is true for dynamical simulations, where studies have shown that different force fields developed for the same system, despite generating similar results in equilibrium uptake simulations, differ greatly in diffusion simulations.[16] This is likely the result of the commonly used procedure of determining gas−zeolite force field parameters to experimental adsorption data primarily through fitting by GCMC simulations, hence, neglecting any potential limiting effects of restricted diffusion on the uptake. In a recent study by some of the authors, a successful attempt was made to combine the thermodynamic and dynamic effects in the uptake of CO$_2$ in Zeolite NaKA[2] in order to explain the results of an experimental uptake study of this material, which yielded an exceptionally high CO$_2$-over-N$_2$ selectivity.[1] Here, a universal-type force field was used as the nature of this study was comparative, and hence, transferability outweighed accuracy. For this current study, it is crucial that the rare-event energy barriers of the pore-to-pore diffusion can be determined accurately in order for the KMC simulations to yield reasonable results because the errors of the computed free-energy barriers are propagated exponentially to the rates of diffusion used as input in the KMC. A more detailed analysis of the propagation of errors is provided in the Supporting Information.

To avoid any problems with unreliable force fields, Density Functional Theory (DFT)-based simulations can be used where accurate and unbiased descriptions of the molecular interactions can be obtained by treating the valence electrons explicitly on a quantum scale. These types of simulations are, however, orders of magnitude more computationally demanding, and we are far from being able to reach the length and time scales of which force field based models are capable. However, if we are able to identify the rate-determining properties for the diffusion of a particular gas molecule through the zeolite, it is possible to compute these different rates on the DFT level of theory and scale up this diffusion information for the different local environments by using the Kinetic Monte Carlo (KMC) method[17−19] to model the rare event dynamics of zeolite pore-to-pore gas diffusion. KMC approaches have been used previously for gas diffusion in zeolites.[17,20,21] However, these studies use force field based Molecular Dynamics (MD) to predict the pore-to-pore diffusion rates, hence the KMC-algorithm is used solely as a way to accelerate the scale of the simulations. In this study, we predict the free-energy barriers of diffusion for the movement of a gas molecule from pore-to-pore in the zeolite using the constrained *ab initio* Molecular Dynamics (AIMD) procedure presented in our previous study.[22]

For the Zeolite NaKA material (structure described in detail in the Supporting Information), we systematically go through certain properties in the material, which we predict to have dominating rate-determining effects. These include: (1) Na^+-to-K^+ extra-framework cation exchange, (2) loading of CO_2, and (3) skin-layer surface defects. In a previous study, we also showed that the mobility of the cations potentially plays a significant role in gas diffusion.[2] We will however leave the further investigation of this aspect for a separate study. This information on the different free-energy barriers for the different local structure properties can then be used to build up a transition-state landscape for a structure with given properties allowing us to perform macroscopic scale KMC diffusion simulations on the system based on information from the DFT level of theory. Hence, using this approach, we are not only coarse graining the time evolution but also actually predicting the transport diffusion through the material. This approach to predicting the diffusion of gas molecules in porous materials is, to our knowledge, the first of its kind and can be implemented on any adsorbate in any porous adsorbent where the diffusion from one pore to another can be considered to be a rare event.

2. COMPUTATIONAL AND MODELING METHODS

In this study, we have developed a true multiscale process, where *ab initio* information is used to model the macroscopic behavior of gas diffusion and uptake rate in a realistic powder particle model. Over the past few years, we have developed a framework for computing the free-energy barriers for the rare event pore-to-pore diffusion of gas molecules in small pore zeolites using constrained AIMD in order to provide accurate input for KMC modeling. From the trajectories of equilibrium AIMD, we estimate the pre-exponential frequency factors in a straightforward manner by computing the frequency at which the gas molecule attempts to enter the respective free-energy barrier region. Additionally, in order to realistically model the gas uptake in porous media with several gas molecules per pore, we have extended the applicability of the conventional lattice-

KMC method, to be applied on geometries with several particles per site.

2.1. Constrained *Ab Initio* Molecular Dynamics— Predicting the Free Energy Barriers of Diffusion. The periodic AIMD simulations performed to compute the free-energy barriers in this study are carried out using the CP2K software.[23] CP2K performs Born−Oppenheimer Molecular Dynamics where the DFT forces are computed "on the fly". The QUICKSTEP module[24,25] is used to implement the GPW method,[26] where augmented plane wave basis sets are combined with atom-centered Gaussian basis sets to accurately and efficiently describe the electron density. For the DFT computations, we used the PBE functional, the DFT-D3 van der Waals correction developed by Grimme[27] to include dispersion forces and the DZVP-MOLOPT-SR basis set[28] to describe the valence electrons, which were treated explicitly while the core electrons were treated effectively using the GTH pseudo potentials[29] for all atom types. A plane wave kinetic energy cutoff of 400 Ry was used.

The simulation cell, shown in Figure 1, was limited to two Zeolite A α-cages, which corresponds to 1/4 crystallographic
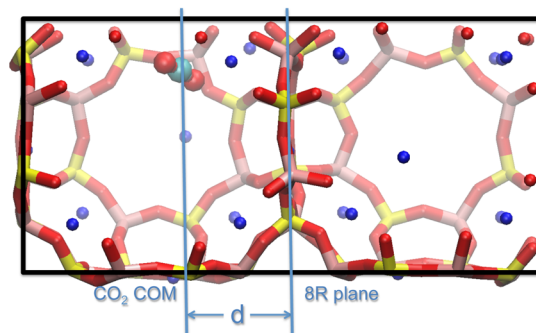
Figure 1. Base simulation cell consisting of two α-cages. One CO_2 molecule is placed in the left α-cage, and a constraint is set confining the distance d between the geometrical center of the gas molecule and the 8-ring window plane intersecting the two α-cages.

unit cell and showed to have negligible effect on the outcome of the performed free-energy barrier computations compared to using a full unit cell periodicity. The original Zeolite A framework geometry was taken from the work of Gramlich and Meier,[30] and the 12 extra-framework Na^+-ions per α-cage were added through a Canonical Monte Carlo simulated annealing energy procedure[31] using the Materials Studio Software suite.[32] With this simulation cell as a base, we then proceeded to alter the local properties within the simulation cell in order to compute how these alternations affect the free-energy barriers of diffusion for CO_2 and N_2 through the 8-ring pore.

Due to the high computational cost of the DFT force computations for each time step in the AIMD, it is necessary to constrain the movement of the gas molecule to the path of interest when computing the free-energy barriers. Here, the path corresponds to the movement through the intersecting 8-ring pore window of the zeolite framework. Using the constraint method,[33,34] implemented according to the procedure presented in some of the authors' recent work,[22] the geometrical center of the gas molecule is spatially constrained in one dimension at a given distance to the plane of the 8-ring pore window as illustrated in Figure 1. This distance is stepwise reduced from 6 to 0 Å with following decreasing intervals; 1 Å down to 3 Å, 0.5 Å down to 1, and

0.25 Å down to 0 Å. For each step, the AIMD is allowed to run for at least 10 ps with a 1.5 fs time step in the NVT-ensemble using the Nosé−Hoover thermostat. The mean force acting on the gas molecule is directly estimated from the time average of the force acting on the geometric constraint, which was converged to a variation tolerance $>1 \times 10^{-4}$ a.u., limiting the statistical errors of the free-energy barriers to ∼1%. The free-energy barriers are then estimated by integrating the force profile of the free-energy barrier region. This is defined to the point-to-plane distance region where the force is nonzero and opposing the gas molecules passage through the pore. For CO_2 passing a Na^+ occupied 8-ring, this region begins at a 2.5 Å point-to-plane distance and 4.0 Å for a K^+ occupied 8-ring as well as for N_2 molecules passing all 8-ring types. The integration region extends to the point where each individual force curve crosses zero, corresponding to the position of the respective barrier, generally at the 8-ring plane ($d = \pm 0.25$ Å).

We start with exchanging the Na^+ ions for K^+ ions at specific sites. We know from the Rietveld refinement powder X-ray diffraction (XRD), presented by Liu et al.[1] and Pluth and Smith,[35] that it is at the 4-ring sites, where the cation exchange takes place first, followed by the 8-ring sites and last the 6-ring Na^+-ions are exchanged to K^+. It should be added that on average only one out of the eight 4-ring sites per α-cage in Zeolite NaA are occupied, whereas all three unique 8-ring and eight 6-ring sites are expected to have full occupancy. Following this, we construct simulation cells with the nine different cation combinations presented in Table 1.

Table 1. Possible Combinations of Na^+/K^+ Cations in the 8-Ring and Surrounding 4- and 6-Rings in Zeolite NaKA

combination no.	4-ring	8-ring	6-ring
1 (base cell)	no ion	Na^+	4 Na^+
2	Na^+	Na^+	4 Na^+
3	K^+	Na^+	4 Na^+
4	no ion	K^+	4 Na^+
5	K^+	K^+	4 Na^+
6	no ion	K^+	3 Na^+ + 1 K^+
7	no ion	K^+	2 Na^+ + 2 K^+
8	no ion	K^+	1 Na^+ + 3 K^+
9	no ion	K^+	4 K^+

The treatment of the combination of K^+ in both the 4-ring and 6-ring sites will be discussed later on.

The next property that is believed to have an effect on the pore-to-pore diffusion is the CO_2 loading. In 2011 Krishna and van Baten[11] predicted with classical MD simulations that the CO_2 diffusion in Si-LTA (containing no cations) decreases with an increased loading. Additionally, in a recent study, Shang et al.[36] used static DFT energy calculations to show that the transition state of a K^+ and Cs^+ ions departing from the 8-ring site is lowered by the presence of additional CO_2 loaded into the CHA pores, in turn, facilitating the pore-to-pore diffusion and uptake of CO_2. Hence, in this study, we wish to further analyze the rate-determining effect of the loading on the pore-to-pore diffusion in Zeolite NaKA. We restrict this study to CO_2 as we expect that the N_2 loading effect is negligible because the uptake of N_2 generally does not exceed one molecule per α-cage in, and the N_2 molecule is relatively inert. This assumption is further supported by Krishna and van Baten's work,[11] where the N_2 diffusion in Si-LTA is shown to be fairly independent of the loading, as well as by the work of

Shang et al.,[36] showing that N_2 had no perturbation effect on transition state of K^+ in the 8-ring site. When investigating this property, it is reasonable to assume that the loading in the pore that the diffusing molecule is diffusing from (the left α-cage in Figure 1) and the loading in pore that the molecule is diffusing to (the right α-cage in Figure 1) have different and possibly opposing effects on the pore-to-pore diffusion of CO_2. As previously shown,[1] the loading capacity in Zeolite NaA corresponds to slightly less than seven CO_2 molecules per α-cage. Hence, we compute the barriers for the pore-to-pore diffusion with loadings up to a maximum of eight CO_2 in either of the pores. To minimize the computational effort, we compute the barriers only for two loading capacities on each side (four and seven CO_2 molecules on the left and right side, respectively, in addition to the diffusing molecule). To estimate the effect of loading for each side, a smoothing curve is extrapolated to fit the two data points for the left and the right pore, respectively, in addition to that of the base cell value as presented in Figure 7. The barrier heights for intermediate loadings are estimated from this curve and presented in Table 5. Additionally, we assume the effect of the loadings in the left and right α-cage, respectively, to be independent of each other. Following this, the deviations from the base cell energy barrier are assumed to be additive when combining loadings from the pores on each side of the 8-ring pore window. We also assume that the loading effect is additive to the effect of the respective pore's ion composition.

2.2. Modeling the Macroscopic Scale Diffusion Using Kinetic Monte Carlo. Kinetic Monte Carlo (KMC) is a modeling method, which evolves the system dynamically from state to state according to a given transition-state landscape. One important difference from atomistic MD is that KMC does not move atoms from one position to another but instead moves the system from one state to another. For rare-event dynamics, the transition-state landscape is defined by the transition rates dominating the dynamics in the system. For the case of CO_2 and N_2 diffusion in Zeolite NaKA, these dominating transition rates correspond to those of the pore-to-pore diffusion. KMC is based in the Arrhenius rate law.

$$k = Ae^{-\Delta E/k_B T} \tag{1}$$

According to the Arrhenius equation (eq 1) we need to define the frequency factor A and the free-energy barrier ΔE for each transition in order to determine the rate constant k for the corresponding transition. Here, A can be interpreted as the frequency at which a gas molecule attempts to cross ΔE and the exponential Boltzmann expression defines the proportion of gas molecules expected to cross ΔE for the corresponding transition at temperature T. Hence, in our system, the rate constant k represents the number of times per unit time a CO_2 or N_2 molecule is expected to cross a pore window with a given free-energy barrier.

For a given temperature there are, hence, two variables, A and ΔE, which are necessary to compute in order to define the rate k_i of a given transition i. The ΔE values for the rate-determining processes are determined according to the previously described approach using constrained AIMD. The pre-exponential frequency factors A are estimated from equilibrium AIMD trajectories for each gas−ion combination. These constraint-free simulations were run for at least 50 ps using the same computational setup as for the constrained simulations however with a full crystallographic unit cell consisting of $2 \times 2 \times 2$ α-cages where each α-cage is loaded

with one gas molecule. Even though this simulation time is too short to observe pore-to-pore diffusion, it is sufficient to gather sufficiently converged statistics for the diffusion of the gas molecules within the α-cage. From these equilibrium AIMD trajectories, A is determined by computing the rate at which the gas molecules pass, in the outward direction, a plane parallel to an 8-ring pore window plane (Figure 2). This plane is
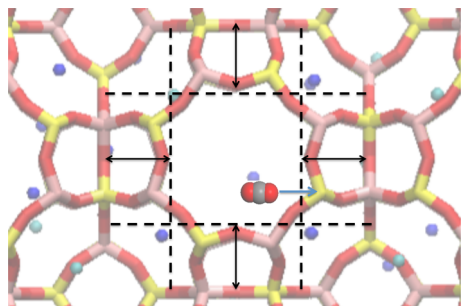
Figure 2. Two-dimensional illustration of the border planes interfacing the free-energy barrier integration region defined to estimate the pre-exponential frequency factors A from equilibrium AIMD simulations by counting how often the respective gas molecule "exits" this border.

positioned at the point-to-plane distance corresponding to the upper limit of free-energy barrier's integration region (2.5 or 4.0 Å). Thus, we compute how often the gas molecule attempts to pass the free-energy barrier. The computed values are presented in Table 2.

Table 2. Computed Pre-Exponential Frequency Factors A in s^{-1} Used To Compute Rates k for KMC-Simulations

	Na$^+$	K$^+$
CO$_2$	5×10^{11}	10×10^{11}
N$_2$	5×10^{11}	5×10^{11}

2.2.1. Lattice-KMC with Several Particles Per Site. Describing diffusion through a porous system with lattice-KMC, where the occupation of gas molecules in each cavity is not restricted to zero or one, poses some technical challenges. The most straightforward way to describe a large cavity with varying occupation of gas molecules in a lattice-KMC simulation, is to use one lattice position for the cavity and let the occupation vary in the simulation. As far as we are aware, there exists no software package that is able to perform such a simulation out of the box. Neither has the theory been outlined how to properly modify the conventional algorithm to correctly account for the double-counting problem that arise when matching processes with local geometries, where several particles are allowed per lattice site. We have here worked out the expressions for summing up the rates correctly, and we implemented our method in the *KMCLib* framework for lattice-KMC simulations.[37,38]

Let us first recall the standard algorithm for lattice KMC simulations as implemented in *KMCLib*.[37] At the start of the simulation, all possible processes are matched against all lattice sites to determine where the processes are available. An elementary process i at site j is selected and executed with a probability $P_{i,j}$ proportional to its rate $R_{i,j}$ in relation to the total available rate in the system $P_{i,j} = R_{i,j}/\sum_{i,j}^{N_i, N_j} R_{i,j}$. Simulation time is then propagated by drawing a time step from an exponentially decreasing distribution, $\Delta t = -\ln(\rho)/\sum_{i,j}^{N_i, N_j} R_{i,j}$,

with the decay given by the total rate $\sum_{i,j}^{N_i, N_j} R_{i,j}$, and ρ is an evenly distributed random number between 0 and 1. The matching between processes and sites is recalculated at the sites affected by the executed event, and the simulation takes another iteration of selecting and executing an event and propagating time. The simulation is stopped after a specified number of iterations.[37] Given that the system can be treated as vibrationally equilibrated at the time an event takes place and given that the program is fed with all relevant processes and correct rates, the KMC algorithm will describe the correct dynamics of the system.[39]

Now, for the KMC algorithm to behave as expected and give rise to the correct dynamics when allowing for more than one particle per lattice site, with correct probabilities for picking a processes and propagating time, we have introduced the concept of *multiplicity* for the process-site matching. If process i matches site j and if there are more than one possibility to perform i at j depending on the number of particles per sites, we call this number of possibilities the *multiplicity* of i at j and denote it by m_{ij}. We aim at defining m_{ij} such that multiplying it with the process rate gives the total available rate for process i at j.

We start out from the conventional algorithm to obtain the total rate for a process, where at the most one particle is present at each lattice site. Here the total available rate for each process is simply the rate for the process times the number of sites where the process is available. Thus, in the case of only one particle per site, m_{ij} equals to one.

Consider now the case when there are more than one particle per site, and look first at the simplest possible case. Let the process i take a particle of type A at site j, and convert it to type B. If the occupation at j is two A when matching, we see that i matches j twice. Hence $m_{ij} = 2$. For a more complex case, let the process i take two particles of type A and convert both to type B, and thus, the occupation at j is five A. Because there are 10 different unique combinations of two A particles that can be drawn from the set of five, there are 10 different ways to perform i at j. Hence $m_{ij} = 10$. Lastly, consider a case where process i takes two particles of type A and three particles of type C and convert them all to type B. If the occupation at j is five A and seven C, we get that $m_{ij} = 350$.

We see that with the number of times r objects can be drawn from n given by the binomial coefficient $\binom{n}{r} = \frac{n!}{r!(n-r)!}$, the multiplicity for process i at a site j is given by the product of the binomial coefficients for each site a and type b in the local geometry common to i and j, where the particles participate in the process. With the occupations denoted $o(i_{a,b})$ and $o(j_{a,b})$, the *multiplicity* is in the general case given by

$$m_{ij} = \prod_{a,b} \binom{o(j_{a,b})}{o(i_{a,b})} \tag{2}$$

The *multiplicity* $m_{i,j}$ of process i at site j thus represents the number of unique possible ways a particular process i can be performed at a particular site j. When allowing for more than one particle per site in the KMC simulations, the rate for the process must be multiplied for each site with m_{ij} when used in the expressions for the picking probability

$$P_{i,j} = (R_{i,j} m_{i,j}) / \sum_{i,j}^{N_i, N_j} (R_{i,j} m_{i,j}) \tag{3}$$

and time step propagation

$$\Delta t = -\ln([0, 1]) / \sum_{i,j}^{N_i, N_j} (R_{i,j} m_{i,j})$$

(4)

We have furthermore combined the concept of *multiplicity* with the expressions in *KMCLib* for site specific rates to use the custom rate calculator framework.[37]

In the particular case of gas diffusion in a porous material we are interested in here, where only one molecule is moved per elementary event, $m_{i,j}$ reduces to the number of molecules of relevant type at the site where the diffusional jump starts.

2.2.2. KMC Simulation Setup. All KMC simulations were performed with the *KMCLib* program.[37] *KMCLib* is an efficient general framework for performing lattice KMC simulations using the *n-fold* way algorithm[40] for selecting and executing events. The input to *KMCLib* is the geometry (lattice and occupation) of the starting structure and a set of possible local events (elementary processes) with corresponding rate constants, and the output is a trajectory describing the system evolving over time.

KMCLib comes with the capability of including on-the-fly rate calculation routines via an API that will be evaluated each time the rate for an elementary process at a specific site needs an update. In this way, the number of elementary events can be kept to a minimum while still allowing flexibility in the definition of the rate expressions. All rates were specified using the on-the-fly rate calculator API.

To be able to simulate gas diffusion through a porous media, with several gas particles allowed per cavity, the above-described additions to the standard KMC algorithm were implemented in *KMCLib*. All modifications made to *KMCLib* to enable these simulations, with more than one particle per site, are available in a development branch in the public *KMCLib* git repository[41] and will become part of a future official update of *KMCLib*.

The KMC simulation cell is constructed to model a Zeolite NaKA cubic powder particle with varying Na^+-to-K^+ ratio composition, Figure 3. Taking the computational effort into account, we limit the modeled powder particle to consist of 23 × 23 × 23 α-cages of 12.3 Å each in addition to a skin layer of surface adsorption cells, hence the total cell dimensions are $a =$
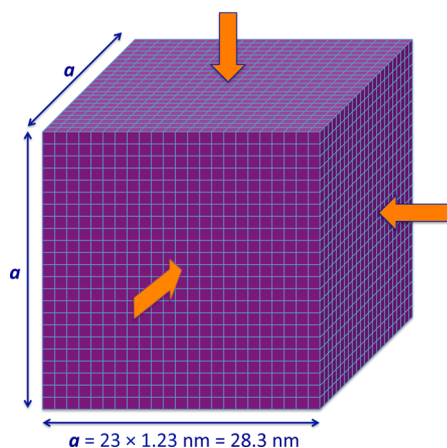
Figure 3. Illustration of the KMC simulation cell set up to model a cubic powder particle. The simulation cell is built up by 25 × 25 × 25 cell units where the outer layer models the skin-layer adsorption surface and the inner core models 23 × 23 × 23 α-cages.

$b = c = 28.3$ nm. The average powder particle size in the experimental work by Liu et al.[1] was estimated to be 4 μm and in order to compare the KMC simulations with the these experimental results, we scale the simulation time by (4 × 10^{-6}m/28.3 × 10^{-9}m)^2 = 2 × 10^4 as the uptake rate typically increases quadratically with increasing particle size.

Each α-cage in the simulation cell is appointed one gas site in the center of the cage ([0, 0, 0]) and three ion sites in the center of the cage-intersecting x-, y-, and z-planes, respectively, corresponding to cage coordinates [0, 0.5, 0.5], [0.5, 0, 0.5], and [0.5, 0.5, 0] of the α-cage. The gas site defines the lattice for the gas molecule dynamics and contains information on the number of CO_2 or N_2 gas molecules in each cage. The ion sites define the combination of ion occupation in and around the 8-ring, which define the barrier. These KMC lattice ion sites should not be confused with the crystallographic ion sites of the Zeolite A structure.

A series of these simulation cells are set up with varying ion compositions to model the Zeolite NaKA powder particles at different K^+-to-Na^+ ratios where the ion combinations are distributed randomly according to respective structure composition. These distributions for each of the modeled levels of K^+-to-Na^+ exchange are presented in Table 3. For N_2, only the 8-ring occupation shows to have a substantial effect on the diffusion rates, *vide infra*. Hence, at 33% Na^+-to-K^+ exchange, all 8-rings are expected to be occupied by K^+, and the lowest diffusion rate should be reached and sustain up to 100% Na^+-to-K^+ exchange. Following this, we limit the KMC simulations to the range 0%–33% Na^+-to-K^+ exchange in the NaKA structure for N_2 with ion compositions according to Table 4.

As the KMC simulations only contain information on the rates of diffusion and cannot predict when the uptake level is in equilibrium at a certain gas pressure, we set an uptake cap of respective gas molecules residing an α-cage for each specific Zeolite NaKA structure composition. These uptake caps were determined from the GCMC simulated equilibrium uptake levels (0.85 bar, 298 K), predicted by Mace et al.,[2] and the cap was set to the closest integer for each corresponding Zeolite NaKA structure composition and gas, respectively. For CO_2, the uptake cap was set to 7/α-cage for the NaA structure composition subsequently decreasing linearly to 2/α-cage for KA. For N_2, however, the GCMC simulated equilibrium uptake corresponded to ~0.5/α-cage for NaA and slightly decreasing with an increasing Na^+-to-K^+ exchange, and hence, the closest upper integer is 1/α-cage for all structure compositions. This overestimates the equilibrium uptake level by 100% or more. To allow a qualitative comparison of the experimental N_2 uptake data with the KMC diffusion simulations with a cap set to 1/α-cage, the KMC-uptake (N_{KMC}) can be scaled by the GCMC equilibrium uptake (N_{GCMC}) according to $N_{scaled} = N_{GCMC} \times N_{KMC}/N_{KMC-NaA}$, where $N_{KMC-NaA}$ corresponds to N_{KMC} for the Zeolite NaA structure composition.

For CO_2, we wish to study the effect that the level of CO_2 loading has on the diffusional uptake rate. To do this, we compare KMC simulations where the diffusion rates are perturbed according to the computed loading effect on the free-energy barriers presented in Table 5, *vide infra*. These are compared with KMC simulations with unperturbed diffusion rates.

The outer skin layer of the simulation cell allows only gas molecule creation and inward diffusion, corresponding to surface adsorption. As the adsorption is an exothermic process,

E

Table 3. Cation Distribution for Different Zeolite NaKA Structure Compositions for KMC Model of CO_2 Diffusion

$K^+/(K^++Na^+)$	0	0.08	0.17	0.33	0.50	0.67	0.83	1
8R = Na^+, 4R = Na^+ [%]	33	0	0	0	0	0	0	0
8R = Na^+ [%]	67	67	44	0	0	0	0	0
8R = Na^+, 4R = K^+ [%]	0	33	22	0	0	0	0	0
8R = K^+, 4R = K^+ [%]	0	0	11	33	31	25	14	0
8R = K^+ [%]	0	0	23	67	69	75	86	100

Table 4. Cation Distribution for Different Zeolite NaKA Structure Compositions for KMC Model of N_2 Diffusion

$K^+/(K^++Na^+)$	0	0.07	0.13	0.20	0.27	0.33
8R = Na^+ [%]	100	80	60	40	20	0
8R = K^+ [%]	0	20	40	60	80	100

the free-energy barrier is negative, and hence, the adsorption rate is many magnitudes higher than the rates of diffusion and should therefore not be rate-limiting for the diffusion and the uptake rate. The presence of skin-layer surface defects as a potentially uptake limiting effect has however been discussed in the recent work by Chueng et al.[42] To investigate this effect, we block a certain percentage of randomly chosen skin-layer surface cells for adsorption, hence limiting the channels of entrance for the gas molecules during the simulations.

Ikeda et al.[43] showed the occurrences of split 6-ring sites in Zeolite KA, protruding on opposite sides of the 6-ring plane either into the α-cage or into the β-cage. According to the XRD, at levels of Na^+-to-K^+ exchange above 33% all 4-ring and 8-ring ions should be exchanged to K^+. Hence, we would expect to see only a linear decrease of the uptake in the range of 33%–100% Na^+-to-K^+ exchange following the decrease of the equilibrium uptake as the Na^+-to-K^+ exchange in the 6-ring sites do not show any substantial effect on the free-energy barriers. To explain this deviation, we suggest that the weakly bound 4-ring K^+ ions may prefer a split 6-ring occupancy for certain ion configurations, hence decreasing the population of K^+ in the 4-ring sites at high levels of Na^+-to-K^+ exchange. To investigate this, we performed DFT geometry optimizations using the same computational setup as for the AIMD simulations, where the stability of the K^+ occupied 4-ring site was tested for three different starting configurations: (1) K^+ occupied the 4-ring site with both neighboring 6-ring sites occupied by Na^+-ions, (2) K^+ occupied the 4-ring site with one of the neighboring 6-ring sites occupied by a Na^+-ion and the other by a K^+-ion, and (3) K^+ occupied the 4-ring site with both neighboring 6-rings occupied by K^+-ions. For cases 1 and 2, the K^+ ion stayed in the 4-ring site, whereas for case 3, the ion relaxed to one of the neighboring 6-rings resulting in a doubly occupied 6-ring. At 50% Na^+-to-K^+ exchange, 3/4 6-ring sites are expected to be occupied by K^+ ions, at 67% 1/2, at 87% 3/4 and at 100% the 6-ring sites are fully occupied by K^+. The number of 6-ring K^+ surrounding a specific 8-ring is expected to follow the binomial distribution as is the probability of 6-ring sites where the K^+ prefers the split 6-ring site over the 4-ring site (case 3), hence reducing the number of 4-ring occupied by K^+ accordingly. This has been taken into account when determining the combination of ion compositions for the KMC simulations, as presented in Table 3.

3. RESULTS AND DISCUSSION

3.1. Free-Energy Barrier Computations. *3.1.1. Cation Exchange.* Figures 4 and 5 show how the force profiles and
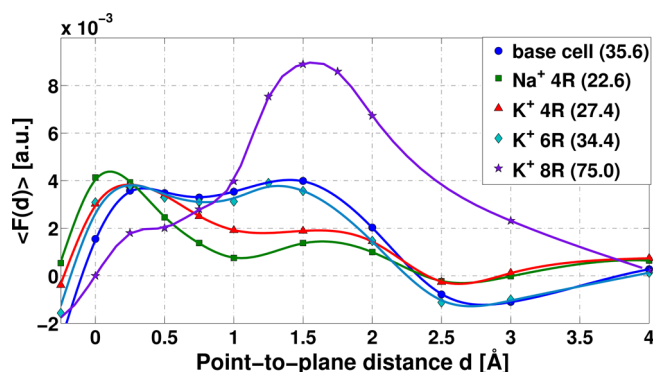
Figure 4. Average force values for CO_2 pore-to-pore diffusion for different ion exchange configurations plotted as a function of the distance d between the 8R-plane and geometrical center of the CO_2 molecule. The computed free-energy barrier values, in kJ/mol, are presented in the parentheses for respective configuration.
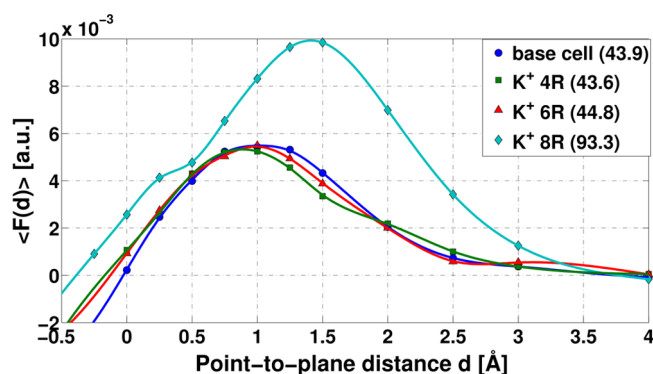
Figure 5. Average force values for N_2 pore-to-pore diffusion for different ion exchange configurations plotted as a function of the distance d between the 8R-plane and geometrical center of the N_2 molecule. The computed free-energy barrier values, in kJ/mol, are presented in the parentheses for respective configuration.

free-energy barriers for CO_2 and N_2 are affected by the ion exchange in the different positions. What is apparent for both CO_2 and N_2 is that the main rate-limiting property is the cation type occupying the 8-ring site. For CO_2, the barrier is 35.6 kJ/mol for Na^+ compared to 75.0 kJ/mol for K^+, and for N_2, the respective barriers are 43.9 and 93.2 kJ/mol; hence, the Na^+-to-K^+ exchange in the 8-ring involves, as expected, a drastic increase in the free-energy barrier of diffusion for both gas molecules. In reality, this would involve a full blockage of CO_2 as well as N_2 diffusion through the K^+ occupied 8-ring within a realistic time scale.

Compared to CO_2, the N_2 barriers are consequently higher (~25%). This is expected following the reasoning of the higher kinetic diameter of N_2, and therefore, the effort to squeeze through the 8-ring pore window is larger. What however showed to be an interesting discovery from this study was the difference in response from the surrounding cation environ-

ment, in particular, the effect of the occupation of the 4-ring site.

From Figure 5, we see that neither the K^+ occupation in the 4-ring site nor the 6-ring site has a significant effect on the force profile or the size of the barrier as compared to the base cell for N_2. CO_2, on the other hand, is strongly effected by the cation occupancy in the 4-ring site, as can be seen from the force profiles in Figure 4, where the forces are drastically perturbed both by the occupation of Na^+ and K^+ at this site. Compared to the base cell, the forces are lowered down to a point-to-plane distance of 0.25 Å, and below this distance, the repulsive force is instead enhanced. However, the overall effects are significant decreases of ~35% and 25% of the barrier to 22.6 and 27.4 kJ/mol for Na^+ and K^+, respectively. On the other hand, when exchanging the Na^+ ion in the 6-ring site to a K^+ ion, the force profile is essentially preserved, and the barrier height is decreased only by 3% to 34.4 kJ/mol. This insignificant effect of the 6-ring occupation observed for the interaction force between the CO_2 molecule and the framework can be rationalized by the 6-ring cation being fairly embedded in the framework "out of the way" of the CO_2 molecule's diffusion path. The 4-ring cation, on the other hand, protrudes from the 4-ring and is also closer to the 8-ring, and therefore, interacts more with the path of diffusion. We also computed the free-energy barrier of diffusion for the CO_2 molecule with K^+ ions occupying both the 8-ring as well as the 4-ring sites because it is known from XRD that the Na^+-to-K^+ exchange first occurs at the 4-ring sites followed by the 8-ring sites. Hence, this combination is of particular interest for moderately low K^+ loading (8−33% K^+ content). Compared to the case when only the 8-ring site is occupied by K^+, a drastic decrease of the free-energy barrier to 46.1 kJ/mol is observed. This decrease could enable the CO_2 diffusion through certain K^+ occupied 8-ring pore windows.

3.1.2. CO_2 Loading. Figure 6 shows the force profiles for the passage of the CO_2 molecule through a Na^+ occupied 8-ring for
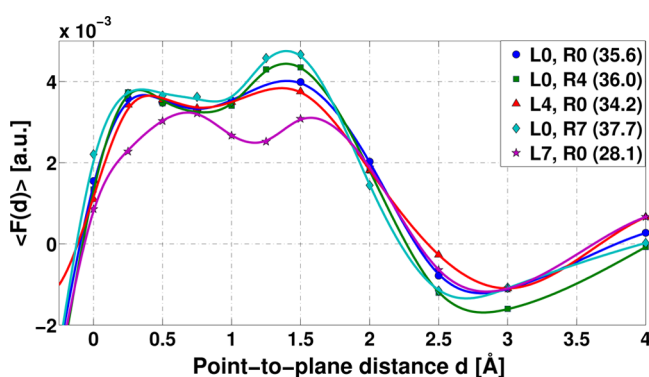
Figure 6. Average force values for CO_2 pore-to-pore diffusion for different CO_2 loadings, in the left and right α-cage of the simulation cell, respectively, plotted as a function of the distance d between the 8R-plane and geometrical center of the CO_2 molecule. The computed free-energy barrier values, in kJ/mol, are presented in the parentheses for respective configuration.

different loadings in the left and the right α-cage, respectively. In Figure 7, we show the extrapolated smoothing spline of the barrier perturbations for the different levels of loading in the two respective cages. These extrapolated relative values $\Delta\Delta E$ as well as the absolute values ΔE are also presented in Table 5.
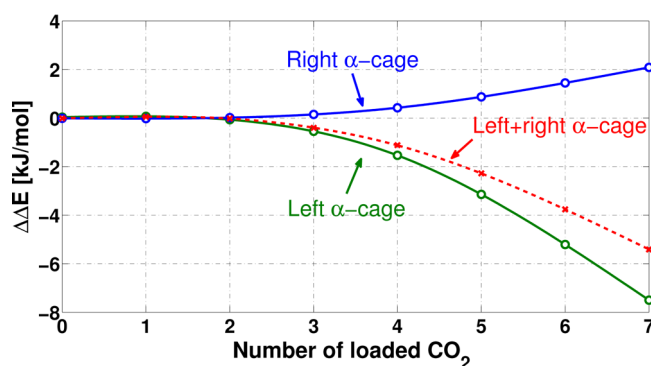
Figure 7. Extrapolated deviations from the base cell free-energy barrier for increasing number of CO_2 molecules loaded in left α-cage (green) and right α-cage (blue), respectively. The red curve shows the sum of these two loadings effects.

Table 5. Computed and Extrapolated Free-Energy Barriers ΔE and Their Deviations from the Base Cell Value $\Delta\Delta E$ for CO_2 Different Numbers of CO_2 Molecules Loaded in the Left (L) and Right (R) α-Cage, Respectively[a]

| no. CO_2 L	no. CO_2 R	ΔE [kJ/mol]	$\Delta\Delta E$ [kJ/mol]
0	**0**	**35.6**	**0.0**
1	0	35.6	0.0
2	0	35.5	−0.1
3	0	35.1	−0.5
4	**0**	**34.2**	**-1.4**
5	0	32.5	−3.1
6	0	30.4	−5.2
7	**0**	**28.1**	**-7.5**
0	**0**	**35.6**	**0.0**
0	1	35.6	0.0
0	2	35.6	0.0
0	3	35.7	0.1
0	**4**	**36.0**	**0.4**
0	5	36.5	0.9
0	6	37.0	1.4
0	**7**	**37.7**	**2.1**

[a]Computed values are given in bold.

From our computations, the free-energy barrier of diffusion for CO_2 in the Zeolite NaA structure is predicted to decrease with an increased loading in the left α-cage while the increased loading in the right α-cage instead results in an increased barrier. These opposing effects can be rationalized by the increased gas pressure and increased collisions toward the diffusing CO_2 molecule in the left α-cage, "helping it" in the process of squeezing through the 8-ring. The opposite effect is then true for the increased gas pressure in the right α-cage. This rate-reducing effect on the diffusion, which the increased loading in the right α-cage poses, is however smaller than the rate-enhancing effect from the left α-cage. One possible explanation could be the interaction between the CO_2 molecules in the right α-cage results in a facilitated diffusion, as predicted by Shang et al.,[36] which reduces the increase of the energy barrier with increased loading in the right α-cage. Hence, as the barrier-decreasing effect is dominant, these results indicate that the CO_2 loading in the Zeolite NaA material has mainly a rate-enhancing effect on the pore-to-pore diffusion.

3.2. KMC Uptake Computations.

Figures 8, 9, and 10 present the KMC modeled uptakes as a function of time for
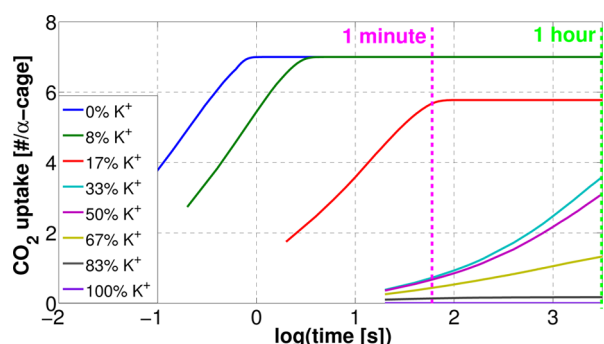
Figure 8. KMC-modeled CO_2 uptake in Zeolite NaKA for different levels of Na$^+$-to-K$^+$ exchange as a function of time excluding CO_2 loading effects.
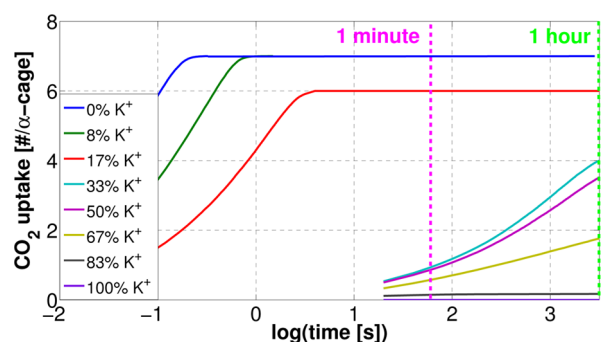
Figure 9. KMC-modeled CO_2 uptake in Zeolite NaKA for different levels of Na$^+$-to-K$^+$ exchange as a function of time including CO_2 loading effects.
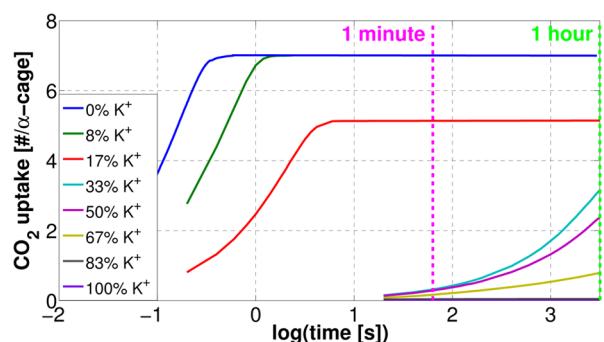
Figure 10. KMC-modeled CO_2 uptake in Zeolite NaKA for different levels of Na$^+$-to-K$^+$ exchange as a function of time including CO_2 loading effects and 75% surface defects.

different levels of Na$^+$-to-K$^+$ exchange excluding the loading effects on the free-energy barriers, including the loading effects, and including 75% surface blockage, respectively.

When analyzing the KMC simulated uptake curves in (Figure 8) where the loading effects on the free-energy barriers have not been taken into account, a fast uptake is predicted for the structure compositions where a certain amount of the 8-ring pores are still occupied by Na$^+$ ions (<33%) and the equilibrium uptake level is reached within a matter of seconds (0% and 8%) or minutes (17%). At Na$^+$-to-K$^+$ exchange levels of 33% and higher, the uptake rates drastically decrease due to the lower diffusion rates through the K$^+$ occupied 8-ring pores

where for 33% Na$^+$-to-K$^+$ exchange 12 h is needed to reach equilibrium. With further increased levels of Na$^+$-to-K$^+$ exchange, this equilibration time increases exponentially with the decreasing levels of the barrier reducing 4-ring occupations in the simulations, and at 100% Na$^+$-to-K$^+$ exchange, it is predicted to take ca. 8 years to reach the predicted equilibrium uptake level.

From Figure 9, showing the KMC simulated uptake curves where the loading perturbation to the free-energy barriers have been included, an accelerated uptake is observed. This effect is particularly significant for low levels of Na$^+$-to-K$^+$ exchange and the equilibration time at 0% K$^+$-content is ca. 4 times faster with the loading effects included. This is explained by the increasing energy barrier lowering effect with increased levels of CO_2 loading as shown in Figure 7, where the highest levels of CO_2 loading are only reached by the structure configurations with the lower levels of Na$^+$-to-K$^+$ exchange.

Figure 10 presents the effect of the modeled surface defects, where 75% of the skin layer has been blocked for adsorption. As expected, the presence of these defects are predicted to decrease the uptake rate and shows particularly to cause a lag in the initial uptake. Compared to the corresponding defect free simulation, the time to reach equilibrium was approximately doubled.

In Figure 11, the level of simulated uptake reached after 1 h for the three different simulation setups described above are
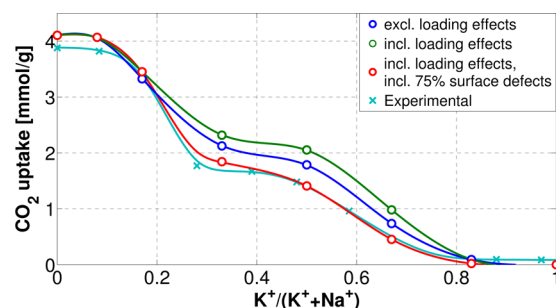
Figure 11. KMC-modeled CO_2 uptake as a function of the level of Na$^+$-to-K$^+$ for the three different simulation setups: excluding effects of CO_2 loading (blue), including effects of CO_2 loading (green), and including the effects of CO_2 loading and including 75% surface defects (red). These are compared to the experimental data from Liu et al.[1] (cyan).

plotted together with the experimental uptake measured by Liu et al.,[1] as a function of the level of Na$^+$-to-K$^+$ exchange. At low levels of Na$^+$-to-K$^+$ exchange, there is no significant difference between the three setups as all reach equilibrium within a matter of minutes. The overestimation of the uptake at 0% and 8% Na$^+$-to-K$^+$ exchange is explained by the uptake cap being set to the closest upper integer (7 CO_2) per α-cage of the estimated equilibrium uptake, resulting in this deviation of approximately 5%. At higher levels of Na$^+$-to-K$^+$ exchange, more significant deviations are observed where the equilibrium uptake levels are not reached within the 1 h time scale, and differences in uptake rates play a significant role. Starting with the initial setup excluding loading effects, the shape resembles that of the experimental measurements; however, at intermediate to high levels of Na$^+$-to-K$^+$ exchange, significant differences from the experimental data are observed, where the uptake is overestimated by 25−30%. It should be added here that it is also for this range (33−67% Na$^+$-to-K$^+$ exchange) that

the computations contain significant uncertainties (5−20%), as shown by the error analysis provided in the Supporting Information. Comparing this initial setup with that including the loading effects, a further increase of the uptake is observed in this range, increasing the deviations from the experimental data to 35%−100%. By adding the effect of substantial skin-layer surface defects, blocking 75% of the skin-layer pores, the uptake is decreased to the experimental levels, showing an excellent agreement.

However, when comparing the experimental adsorption kinetics data presented by Cheung et al.[3] for 0% and 17% Na$^+$-to-K$^+$ exchange showing that 90% of the uptake capacities were reached at 22 and 125 s, respectively, to 0.3 and 3 s according to the corresponding KMC simulations, it is clear that the KMC predicts substantially higher uptake rates, at least for low levels of Na$^+$-to-K$^+$ exchange.

Figures 12 and 13 show the KMC simulated uptake for N$_2$ without and with 75% skin-layer defects, respectively, for
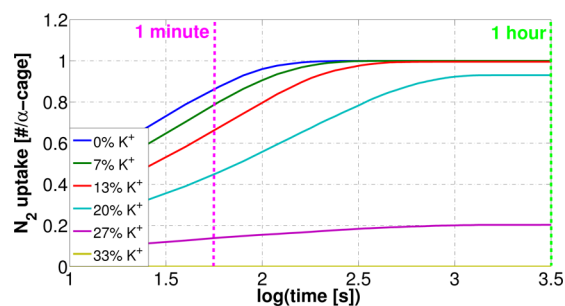

Figure 12. KMC-modeled N$_2$ uptake in Zeolite NaKA for different levels of Na$^+$-to-K$^+$ exchange as a function of time.
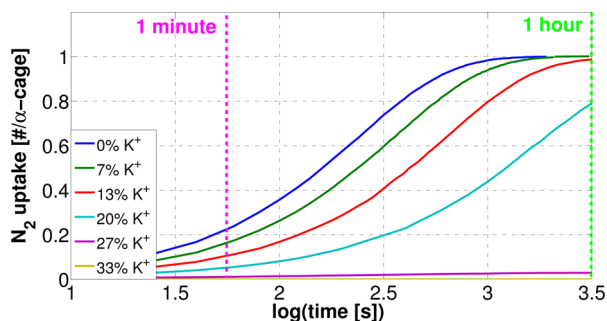
Figure 13. KMC-modeled N$_2$ uptake in Zeolite NaKA for different levels of Na$^+$-to-K$^+$ exchange as a function of time, including 75% surface defects.

different levels of Na$^+$-to-K$^+$ exchange. For the defect-free simulation setup, the set equilibrium level loading is reached within the 1 h limit by compositions up to 13% Na$^+$-to-K$^+$ exchange where the pure NaA composition (0% Na$^+$-to-K$^+$ exchange) takes 5 min to reach the set equilibrium level. When including the 75% skin-layer defects, the same trend as for CO$_2$ is observed, resulting in lowered uptake rates and longer equilibration times. Here, the equilibration time is increased to 30 min for the NaA structure.

Figure 14 shows the level of uptake reached after the 1 h limit, with and without scaling by the GCMC simulated levels of equilibrium, together with the experimental values[1] as a function of the level of Na$^+$-to-K$^+$ exchange. The simulated uptake drop at 15−20% cation exchange is steeper and slightly later occurring than the experimental one (5−15%). This is
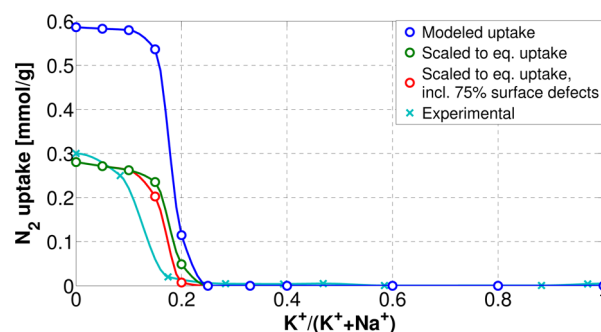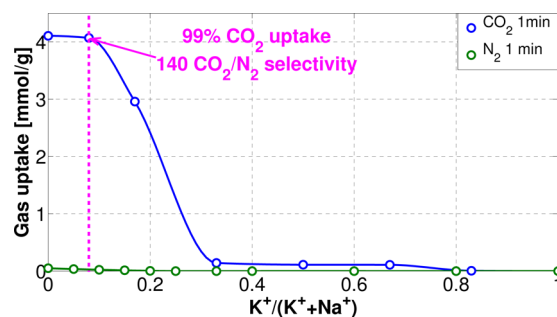

Figure 14. KMC-modeled CO$_2$ uptake after 1 h plotted as a function of the level of Na$^+$-to-K$^+$ for the three different simulation setups: excluding effects of CO$_2$ loading (blue), including effects of CO$_2$ loading (green) and including the effects of CO$_2$ loading and including 75% surface defects (red). These are compared to the experimental data from paper I (cyan).

partly corrected by the addition of surface defects shifting the simulated curve drop to range between 10 and 20% exchange. Despite these deviations, the simulations have a qualitatively excellent agreement with the experimental data.

For cyclic industrial separation processes, such as temperature or pressure swing adsorption techniques, rapid adsorption dynamics are necessary for fast and efficient swing cycles, preferably <5 min. Akhtar et al.[44] proposed a figure of merit F to predict a material's performance as a sorbent. According to eq 5, this measure depends on the CO$_2$-over-N$_2$ selectivity S_{CO_2/N_2} as defined by the ideal adsorption solution theory as well as the CO$_2$ uptake at time τ, hence taking adsorption kinetics into account.

$$F = \frac{S_{CO_2/N_2} N_{CO_2}}{\tau} \tag{5}$$

For 1 min cycles, Zeolite NaKA with a 9.9% Na$^+$-to-K$^+$ exchange, showed the best performance according to this figure of merit. Figure 15 shows the KMC-simulated CO$_2$ and

Figure 15. KMC modeled CO$_2$ uptake after 1 min plotted as a function of the level of Na$^+$-to-K$^+$.

N$_2$ uptakes after 1 min. These results show a high selectivity at 8% Na$^+$-to-K$^+$ exchange, whereas the level of CO$_2$ uptake yet reaches the full equilibrium level, and the computed F is 30% higher than that at the 17% exchange level. Hence, our results agree with those of Akhtar et al., showing that a Na$^+$-to-K$^+$ exchange close to 10% is preferential over the 17% level, despite lower selectivities, which is due to the faster adsorption kinetics at the lower levels of Na$^+$-to-K$^+$ exchange.

4. CONCLUSIONS AND OUTLOOK

Using constrained AIMD, we have identified important rate-determining properties for the diffusion of CO_2 and N_2 in Zeolite NaKA by computing and comparing the free-energy barriers for the pore-to-pore diffusion in different local environments. Further, we have presented a viable approach to coarse grain this microscopic scale information predicted on the electronic scale level of theory on a picosecond time scale, to macroscopic length and time scales in a realistic model, allowing a direct comparison with experimental uptake and kinetic results. Using this methodology applicable to any guest molecule in any porous material where the pore-to-pore diffusion can be defined as a rare event, we can test the effects of different properties predicted to be rate-determining on the diffusion driven uptake and test models to explain certain uptake behavior.

In this work, we demonstrate the effects of cation exchange, CO_2 loading, and skin-layer surface defects. Additionally, we suggest a model by combining these effects, successfully reproducing the experimental uptake dependence of Zeolite NaKA on the level of Na^+-to-K^+ exchange presented by Liu et al.[1] Our simulations, however, show adsorption kinetics for low levels of Na^+-to-K^+ exchange, which are much faster than those measured experimentally.[42] This indicates that there are more, potentially rate-determining properties, to be identified and tested. For example, factors such as internal surface defects, heat transfer from the exothermic surface adsorption, and presence of water have been suggested to explain why similar crystals exhibit different uptake kinetics, as shown in a recent paper by Ruthven.[45] More complex models consisting of several phases with different locally dependent properties in addition to macroscopic condition variations simulating realistic system conditions are possible with the flexible KMC-model as implemented by *KMClib* and are planned for future work.

■ ASSOCIATED CONTENT

Ⓢ Supporting Information

The Supporting Information is available free of charge on the ACS Publications website at DOI: 10.1021/acs.jctc.5b00401.

> Zeolite NaKA structure information and error analysis details (PDF)
> Structural information (ZIP)

■ AUTHOR INFORMATION

Corresponding Author

*E-mail: aatto.laaksonen@mmk.su.se.

Notes

The authors declare no competing financial interest.

■ ACKNOWLEDGMENTS

■ REFERENCES

(1) Liu, Q.; Mace, A.; Bacsik, Z.; Sun, J.; Laaksonen, A.; Hedin, N. *Chem. Commun.* **2010**, *46*, 4502−4504.

(2) Mace, A.; Hedin, N.; Laaksonen, A. *J. Phys. Chem. C* **2013**, *117*, 24259−24267.

(3) Cheung, O.; Bacsik, Z.; Krokidas, P.; Mace, A.; Laaksonen, A.; Hedin, N. *Langmuir* **2014**, *30*, 9682−9690.

(4) García-Sánchez, A.; Ania, C. O.; Parra, J. B.; Dubbeldam, D.; Vlugt, T. J. H.; Krishna, R.; Calero, S. *J. Phys. Chem. C* **2009**, *113*, 8814−8820.

(5) Pillai, R. S.; Peter, S. A.; Jasra, R. V. *Langmuir* **2007**, *23*, 8899−8909.

(6) Maurin, G.; Belmabkhout, Y.; Pirngruber, G.; Gaberova, L.; Llewellyn, P. *Adsorption* **2007**, *13*, 453−460.

(7) Maurin, G.; Llewellyn, P. L.; Bell, R. G. *J. Phys. Chem. B* **2005**, *109*, 16084−16091.

(8) Jaramillo, E.; Chandross, M. *J. Phys. Chem. B* **2004**, *108*, 20155−20159.

(9) Akten, E. D.; Siriwardane, R.; Sholl, D. S. *Energy Fuels* **2003**, *17*, 977−983.

(10) Krishna, R.; van Baten, J. M. *Microporous Mesoporous Mater.* **2009**, *125*, 126−134.

(11) Krishna, R.; van Baten, J. M. *Microporous Mesoporous Mater.* **2011**, *137*, 83−91.

(12) Madison, L.; Heitzer, H.; Russell, C.; Kohen, D. *Langmuir* **2011**, *27*, 1954−1963.

(13) Fang, H.; Kamakoti, P.; Zang, J.; Cundy, S.; Paur, C.; Ravikovitch, P. I.; Sholl, D. S. *J. Phys. Chem. C* **2012**, *116*, 10692−10701.

(14) Fischer, M.; Bell, R. G. *J. Phys. Chem. C* **2012**, *116*, 26449.

(15) Fang, H.; Kamakoti, P.; Ravikovitch, P. I.; Aronson, M.; Paur, C.; Sholl, D. S. *Phys. Chem. Chem. Phys.* **2013**, *15*, 12882−12894.

(16) García-Sánchez, A.; van den Bergh, J.; Castillo, J. M.; Calero, S.; Kapteijn, F.; Vlugt, T. J. H. *Microporous Mesoporous Mater.* **2012**, *158*, 64−76.

(17) Auerbach, S. *Int. Rev. Phys. Chem.* **2000**, *19*, 155−198.

(18) Voter, A. *NATO Sci. Ser.* **2007**, *235*, 1−23.

(19) Kratzer, P. *NIC Series* **2009**, *42*, 51−76.

(20) Krishna, R.; van Baten, J. M. *Chem. Eng. Technol.* **2005**, *28*, 160−167.

(21) Abouelnasr, M. K. F.; Smit, B. *Phys. Chem. Chem. Phys.* **2013**, *14*, 11600−11609.

(22) Mace, A.; Laasonen, K.; Laaksonen, A. *Phys. Chem. Chem. Phys.* **2014**, *16*, 166−172.

(23) CP2K, version 2.4.0. 2013. http://www.cp2k.org/ (accessed August 7, 2015).

(24) Krack, M.; Parrinello, M. *NIC Series* **2004**, *25*, 29−51.

(25) VandeVondele, J.; Krack, M.; Mohamed, F.; Parrinello, M.; Chassaing, T.; Hutter, J. *Comput. Phys. Commun.* **2005**, *167*, 103−128.

(26) Lippert, G.; Hutter, J.; Parrinello, M. *Theor. Chem. Acc.* **1999**, *103*, 124−140.

(27) Grimme, S.; Antony, J.; Ehrlich, S.; Krieg, H. *J. Chem. Phys.* **2010**, *132*, 154104−154122.

(28) VandeVondele, J.; Hutter, J. *J. Chem. Phys.* **2007**, *127*, 114105−114113.

(29) Goedecker, S.; Teter, M.; Hutter, J. *Phys. Rev. B: Condens. Matter Mater. Phys.* **1996**, *54*, 1703.

(30) Gramlich, V.; Meier, W. M. *Z. Kristallogr. - Cryst. Mater.* **1971**, *133−149*, 139−149.

(31) Kirkpatrick, S.; Gelatt, C. D.; Vecchi, M. P. *Science* **1983**, *220*, 671−680.

(32) Materials Studio, version 7.0, Accelrys Software Inc. 2013. www.accelrys.com/products/materials-studio (accessed August 7, 2015).

(33) Sprik, M.; Ciccotti, G. *J. Chem. Phys.* **1998**, *109*, 7737.

(34) Carter, E. A.; Ciccotti, G.; Hynes, J. T.; Kapral, R. *Chem. Phys. Lett.* **1989**, *156*, 472.

(35) Pluth, J. J.; Smith, J. V. *J. Am. Chem. Soc.* **1980**, *102*, 4704−4708.

(36) Shang, J.; Li, G.; Singh, R.; Gu, Q.; Nairn, K.; Bastow, T.; Medhekar, N.; Doherty, C. M.; Hill, A. J.; Liu, J. Z.; Webley, P. A. *J. Am. Chem. Soc.* **2012**, *134*, 19246−19253.

(37) Leetmaa, M.; Skorodumova, N. V. *Comput. Phys. Commun.* **2014**, *185*, 2340.

(38) Leetmaa, M., Skorodumova, N. V. *Comput. Phys. Commun.* **2015**, *in press*.

(39) Fichthorn, K. A.; Weinberg, W. H. *J. Chem. Phys.* **1991**, *95*, 1090−1096.

(40) Bortz, A. B.; Kalos, M. H.; Lebowitz, J. L. *J. Comput. Phys.* **1975**, *17*, 10−18.

(41) Leetmaa, M. *KMClib git repository.* https://github.com/leetmaa/KMCLib (accessed Aug 7, 2015).

(42) Cheung, O.; Bacsik, Z.; Liu, Q.; Mace, A.; Hedin, N. *Appl. Energy* **2013**, *112*, 1326−1336.

(43) Ikeda, T.; Kodaira, T.; Oh, T.; Nisawa, A. *Microporous Mesoporous Mater.* **2002**, *57*, 249−261.

(44) Akhtar, F.; Liu, Q.; Hedin, N.; Bergström, L. *Energy Environ. Sci.* **2012**, *5*, 7664−7673.

(45) Ruthven, D. M. *Microporous Mesoporous Mater.* **2012**, *162*, 69−79.